Journal of Solid State Chemistry 182 (2009) 273–279

Contents lists available at ScienceDirect

Journal of Solid State Chemistry

journal homepage: www.elsevier.com/locate/jssc

Structural and magnetic properties of the quaternary oxides $Ba_6Ln_2Fe_4O_{15}$ (Ln = Pr and Nd)

Kyosuke Abe [a], Yoshihiro Doi [a,*], Yukio Hinatsu [a], Kenji Ohoyama [b]

[a] Division of Chemistry, Graduate School of Science, Hokkaido University, Sapporo 060-0810, Japan
[b] Institute for Materials Research, Tohoku University, Sendai 980-8577, Japan

ARTICLE INFO

Article history:
Received 31 July 2008
Received in revised form
18 October 2008
Accepted 23 October 2008
Available online 5 November 2008

Keywords:
$Ba_6Nd_2Al_4O_{15}$-type structure
Magnetic cluster
Magnetic transition
Powder neutron diffraction
Honeycomb lattice

ABSTRACT

The crystal structures and magnetic properties of the quaternary lanthanide oxides $Ba_6Ln_2Fe_4O_{15}$ (Ln = Pr and Nd) are reported. They crystallize in a hexagonal structure with space group $P6_3mc$ and have the "Fe_4O_{15} cluster" consisting of one FeO_6 octahedron and three FeO_4 tetrahedra. Measurements of the magnetic susceptibility, specific heat, and powder neutron diffraction reveal that this cluster behaves as a spin tetramer with a ferrimagnetic ground state of $S_T = 5$ even at room temperature. The cluster moments show a long-range antiferromagnetic ordering at 23.2 K (Ln = Pr) and 17.8 K (Nd), and the magnetic moments of the Ln^{3+} ions also order cooperatively. By applying the magnetic field (~2 T), this antiferromagnetic ordering of the clusters changes to a ferromagnetic one. This result indicates that there exists a competition in the magnetic interaction between the clusters.

1. Introduction

The magnetic properties of metal ion clusters separated by shells of organic ligand molecules are attracting a great deal of interest since they often show anomalous magnetic properties like the single molecular magnets, e.g., $[Mn_{12}O_{12}(CH_3COO)_{16}(H_2O)_4]$ [1,2]. In solid-state oxides, the cluster-like magnetic behavior is observed when the magnetic interaction between magnetic ions belonging to same cluster is much stronger than that belonging to different clusters. For example, the ruthenium dimer in 6H-perovskites $Ba_3MRu_2O_9$ (M = Mg, Ca, Cd, and Sr) [3,4] and the copper trimer in the $La_4Cu_3MoO_{12}$ [5,6] show characteristic magnetic properties reflecting a strong antiferromagnetic interaction in the cluster.

In order to explore further interesting materials, we have paid attention to the magnetic properties of the $Ba_6Ln_2Fe_4O_{15}$ (Ln = La, Pr, and Nd) [7–11] with the $Ba_6Nd_2Al_4O_{15}$-type structure [12]. In these compounds, one FeO_6 octahedron and three FeO_4 tetrahedra connected via the corner oxygen and the Fe_4O_{15} cluster are formed. Our recent study for $Ba_6La_2Fe_4O_{15}$ showed that the Fe_4O_{15} cluster behaves as a spin tetramer with a ferrimagnetic ground state of the total spin $S_T = 5$ [11]. At 12.8 K, this compound shows a magnetic transition due to the antiferromagnetic ordering of the cluster moments. The determined antiferromagnetic structure is not simple and indicates the existence of a competition in the magnetic interaction between clusters.

For the isostructural $Ba_6Pr_2Fe_4O_{15}$ and $Ba_6Nd_2Fe_4O_{15}$, no detailed magnetic properties are known except for the Néel temperatures (21 and 14 K, respectively) [9]. These compounds contain the magnetic Ln^{3+} ions located at a site surrounding the Fe_4O_{15} cluster, which may exert great influence on the nature of the cluster itself and its magnetic interaction. In this study, we investigated the crystal structures and magnetic properties of $Ba_6Pr_2Fe_4O_{15}$ and $Ba_6Nd_2Fe_4O_{15}$ in detail. The results of their magnetic susceptibility, magnetization, specific heat, and powder X-ray and neutron diffraction measurements are reported.

2. Experimental

Polycrystalline samples of $Ba_6Pr_2Fe_4O_{15}$ and $Ba_6Nd_2Fe_4O_{15}$ were synthesized by the standard solid-state reaction. As starting materials, $BaCO_3$, Pr_6O_{11}, Nd_2O_3 (dried at 1173 K overnight), and Fe_2O_3 were used. They were weighed out in the appropriate metal ratios and well mixed in an agate mortar. The mixtures were pressed into pellets and then calcined at 1173 K for 12 h, and fired at 1573 K for 24 h in air with intermediate grindings and pelletings. The $Ba_6Pr_2Fe_4O_{15}$ sample for neutron diffraction measurements contains a small amount (~1%) of unknown impurity.

The reaction products were characterized by powder X-ray diffraction measurements. The data were obtained by using a Rigaku MultiFlex diffractometer with graphite-monochromated Cu$K\alpha$ radiation in the range $10^\circ \leqslant 2\theta \leqslant 120^\circ$ ($\Delta 2\theta = 0.02^\circ$). Powder neutron diffraction measurements were performed at 2.5 and 50 K in the range $3^\circ \leqslant 2\theta \leqslant 153^\circ$ at intervals of 0.1° with the wavelength

* Corresponding author. Fax: +81 11 706 4931.
E-mail address: doi@sci.hokudai.ac.jp (Y. Doi).

0022-4596/$ - see front matter © 2008 Elsevier Inc. All rights reserved.
doi:10.1016/j.jssc.2008.10.022

of 1.81424 Å, using the Kinken powder diffractometer for high efficiency and high resolution measurement, HERMES, of the Institute for Materials Research (IMR), Tohoku University [13], installed at the JRR-3M reactor in the Japan Atomic Energy Agency (JAEA), Tokai. The X-ray and neutron diffraction data were analyzed by the Rietveld technique, using the program RIETAN2000 [14].

The magnetic measurements were carried out using the SQUID magnetometer (Quantum Design, MPMS-5S). The temperature dependence of magnetic susceptibilities was measured under both zero-field-cooled (ZFC) and field-cooled (FC) conditions in an applied field of 0.1 T over the temperature range 1.8–400 K. The field dependence of magnetization was measured at 1.8 K by changing the applied magnetic field between 0 and 5 T.

The specific heat measurements were performed using a relaxation technique supplied by the commercial specific measurement system (Quantum Design, PPMS) in the temperature range 1.8–300 K. The sintered sample in the form of pellet (~10 mg) was mounted on an alumina plate with apiezon for better thermal contact.

3. Results and discussion

3.1. Crystal structure

The X-ray diffraction profiles at room temperature show that $Ba_6Pr_2Fe_4O_{15}$ and $Ba_6Nd_2Fe_4O_{15}$ are formed as single-phase materials. Both data could be completely explained by using a structural model for the $Ba_6Nd_2Al_4O_{15}$ (space group $P6_3mc$) [12]. The schematic crystal structure for the $Ba_6Ln_2Fe_4O_{15}$ is illustrated in Fig. 1(a). The lattice parameters at room temperature were determined to be $a = 11.8533(6)$ Å and $c = 7.0655(3)$ Å (for Ln = Pr) and $a = 11.8292(5)$ Å and $c = 7.0436(2)$ Å (Nd). These values are in good agreement with the previous results [8–10].

The powder neutron diffraction profiles for $Ba_6Pr_2Fe_4O_{15}$ and $Ba_6Nd_2Fe_4O_{15}$ are plotted in Figs. 2 and 3. All of the nuclear Bragg peaks show that both compounds keep the hexagonal structure down to 2.5 K, i.e., no evidence for a structural phase transition was found. The profiles at 2.5 K also show the magnetic Bragg peaks indicating the occurrence of the long-range magnetic ordering, which will be discussed later.

The neutron diffraction data were analyzed by the Rietveld method; the refined structural parameters are summarized in Tables 1 and 2. Some bond lengths calculated from these parameters are listed in Table 3. In the $Ba_6Nd_2Al_4O_{15}$-type structure [12], the Ba^{2+} ions occupy four kinds of crystallographic sites, Ba(1), Ba(2), Ba(3), and Ba(4), with the coordination numbers of 6, 10, 12, and 8, respectively. These coordination polyhedra are illustrated in Fig. 1(b) and (c). The values of the bond valence sum (BVS) [15] were calculated, and the results are also listed in Table 3. The value for Ba(1), Ba(2), Ba(3) sites are approximately close to 2, which is reasonable for the divalent ion. On the other hand, that for the Ba(4) site is much larger than 2. This result is due to the fact that smaller Ln^{3+} ions also occupy this site in a disordered manner (the ratio is Ba:Ln = 1:2). We checked a possibility of partial occupation of other barium sites by Ln ions; however, such evidence was not found.

The Fe ions occupy two crystallographic sites (2b and 6c) surrounded by six and four oxygen ions (see Fig. 1(a) and Table 3); their BVS values (~3) indicate that the Fe ions are in the trivalent state. In the crystal structure of $Ba_6Ln_2Fe_4O_{15}$, it is notable that one $Fe(1)O_6$ octahedron and three $Fe(2)O_4$ tetrahedra form a lager unit "Fe_4O_{15} cluster" by corner-sharing. The shortest Fe–Fe distance is ~4.07 Å for Fe(1)–Fe(2) in the cluster; these cations are linked via an intermediate O(2) ion. The other Fe–Fe distances are longer than ~5.06 Å and are linked through two or more oxygen ions.

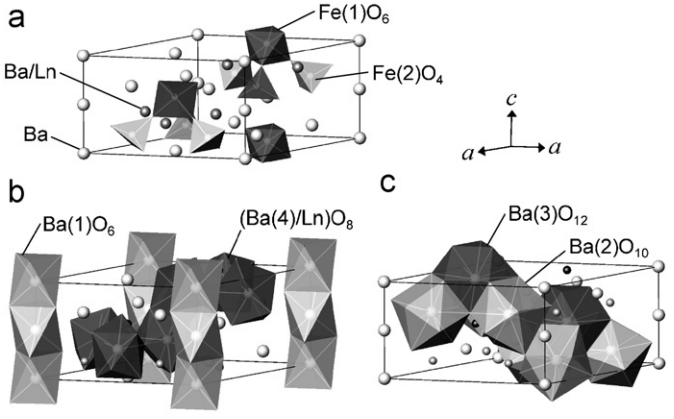

Fig 1. Schematic crystal structure of $Ba_6Ln_2Fe_4O_{15}$. The coordination polyhedra for (a) $Fe(1)O_6$ and $Fe(2)O_4$, (b) $Ba(1)O_6$ and Ba(4)/LnO_8, and (c) $Ba(2)O_{12}$ and $Ba(3)O_{10}$. Oxygen ions are omitted.

3.2. Magnetic susceptibility

Fig. 4 shows the temperature dependence of the inverse magnetic susceptibilities for $Ba_6Pr_2Fe_4O_{15}$ and $Ba_6Nd_2Fe_4O_{15}$. For comparison, data for $Ba_6La_2Fe_4O_{15}$ [11] are also plotted. They cannot be simply explained by the Curie–Weiss law owing to a poor linearity at high temperature region. The effective magnetic moments per formula unit at room temperature are 8.96 (for Ln = La), 10.22 (Pr), and 10.28 μ_B (Nd). Assuming the free-ion value for the Ln^{3+} ion (3.58 μ_B for Pr^{3+} and 3.62 μ_B for Nd^{3+}), the contribution from four Fe^{3+} ions is estimated to be 8.96, 8.88, and 8.92 μ_B, respectively. These values agree well with each other; however, they are significantly smaller than the value for the free Fe^{3+} ion ($S = 5/2$): $\sqrt{4\mu^2_{Fe3+}} = 11.83\,\mu_B$. This result means that the magnetic moments of Fe^{3+} ions are not free even at room temperature.

Our recent study for $Ba_6La_2Fe_4O_{15}$ [11] showed that the temperature dependence of the magnetic susceptibility could be explained as a paramagnetic behavior of not the free Fe^{3+} ions but the ferrimagnetic Fe_4O_{15} clusters (Fig. 5). This result is derived from its structural feature, i.e., the strong superexchange pathway (linear Fe–O–Fe) exists only in the cluster. This relation should be applicable to the isostructural $Ba_6Pr_2Fe_4O_{15}$ and $Ba_6Nd_2Fe_4O_{15}$. Therefore, the isolated cluster model used for the La compound [11] was applied to them. In this model, the exchange Hamiltonian in the cluster is represented as

$$H_{ex} = -2J_1(\mathbf{S}_1\mathbf{S}_2 + \mathbf{S}_1\mathbf{S}_3 + \mathbf{S}_1\mathbf{S}_4) - 2J_2(\mathbf{S}_2\mathbf{S}_3 + \mathbf{S}_2\mathbf{S}_4 + \mathbf{S}_3\mathbf{S}_4) \quad (1)$$

where $\mathbf{S}_i$ and J_i denote the spin angular momentum for the Fe^{3+} ion and the exchange integral between Fe^{3+} ions (see Fig. 5). The molar magnetic susceptibility of the Fe_4O_{15} cluster is given by the Van–Vleck equation:

$$\chi_{cluster} = \frac{N_A g^2 \mu_B^2 \sum_{S_T,S'} S_T(S_T+1)(2S_T+1)\, e^{-E(S_T,S')/k_BT}}{3k_BT \sum_{S_T,S'} (2S_T+1)\, e^{-E(S_T,S')/k_BT}} \quad (2)$$

where N_A, g, and k_B are Avogadro number, g-factor (= 2.0), and Boltzmann constant, respectively; $E(S_T, S')$, S_T, and S' mean the eigenvalues of Eq. (1), spin quantum numbers for $\mathbf{S}_T = \mathbf{S}_1+\mathbf{S}_2+\mathbf{S}_3+\mathbf{S}_4$ and $\mathbf{S}' = \mathbf{S}_2+\mathbf{S}_3+\mathbf{S}_4$, respectively.

In the case of $Ba_6Pr_2Fe_4O_{15}$ and $Ba_6Nd_2Fe_4O_{15}$, paramagnetic Ln^{3+} ions also contribute to the magnetic susceptibility. This contribution is added to the molar magnetic susceptibility as a

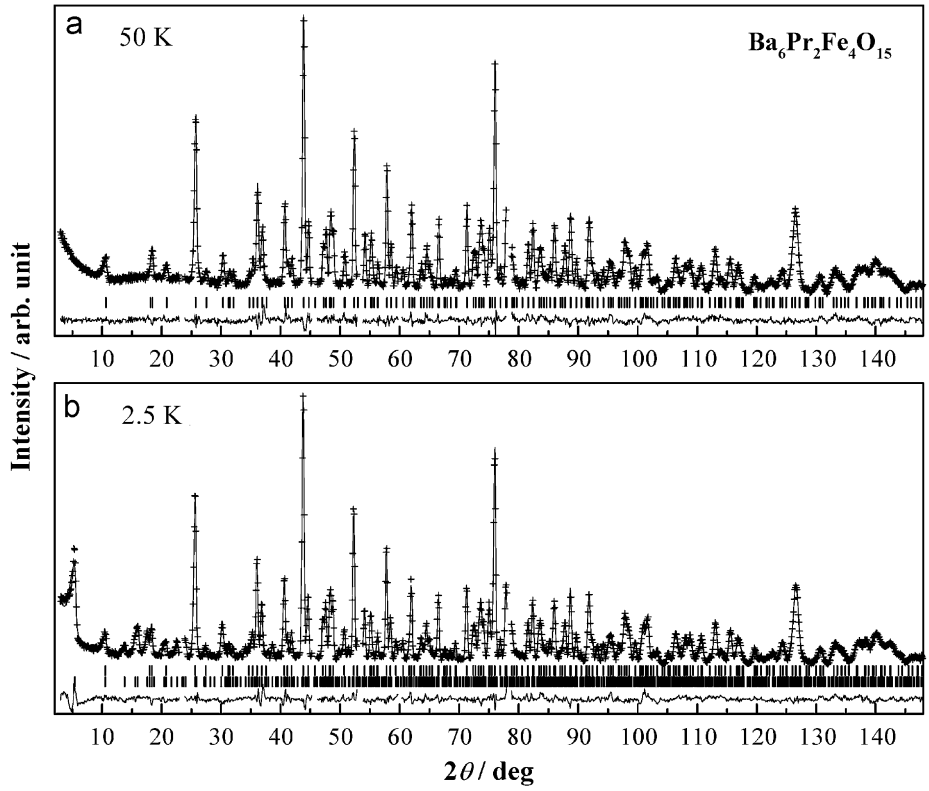

Fig. 2. Powder neutron diffraction profiles for $Ba_6Pr_2Fe_4O_{15}$ at (a) 50 K and (b) 2.5 K. The vertical marks represent the peak positions (a) for nuclear reflection and (b) for nuclear (upper) and magnetic (lower) reflections.

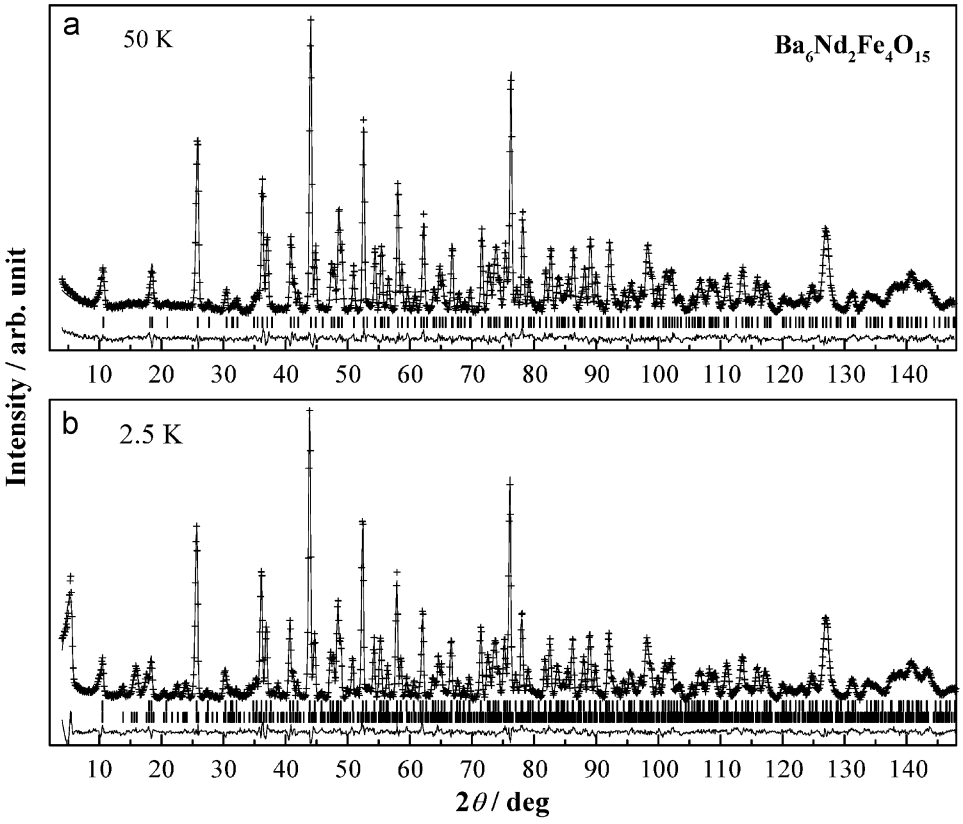

Fig. 3. Powder neutron diffraction profiles for $Ba_6Nd_2Fe_4O_{15}$ at (a) 50 K and (b) 2.5 K. The vertical marks represent the peak positions (a) for nuclear reflection and (b) for nuclear (upper) and magnetic (lower) reflections.

Table 1
Structural parameters for $Ba_6Pr_2Fe_4O_{15}$ determined by the neutron diffraction measurements at 50 and 2.5 K.

Atom	Site	Occupancy	x	y	z	B/Å^2
$T = 50$ K						
Space group $P6_3mc$; $a = 11.8416(6)$ Å; $c = 7.0391(3)$ Å						
$R_{wp} = 4.76\%$; $R_e = 3.12\%$; $R_I = 1.64\%$						
Ba(1)	2*a*	1.0	0	0	0[a]	0.35 (8)
Ba(2)	6*c*	1.0	0.1739 (3)	0.8261	0.1584 (17)	0.35
Ba(3)	2*b*	1.0	1/3	2/3	0.4760 (18)	0.35
Ba(4)	6*c*	0.33333	0.4784 (3)	0.5216	0.8272 (16)	0.35
Pr	6*c*	0.66667	0.4784	0.5216	0.8272	0.35
Fe(1)	2*b*	1.0	1/3	2/3	0.0213 (17)	0.62 (7)
Fe(2)	6*c*	1.0	0.1774 (1)	0.8226	0.6606 (16)	0.62
O(1)	12*d*	1.0	0.6746 (5)	0.0653 (4)	0.0245 (15)	1.2 (1)
O(2)	6*c*	1.0	0.2501 (3)	0.7499	0.8388 (19)	1.2
O(3)	6*c*	1.0	0.4139 (3)	0.5861	0.1683 (18)	1.2
O(4)	6*c*	1.0	0.9029 (3)	0.0971	0.2704 (18)	1.2
$T = 2.5$ K						
Space group $P6_3mc$; $a = 11.8316(5)$ Å; $c = 7.0326(3)$ Å						
$R_{wp} = 4.76\%$; $R_e = 2.45\%$; R_I (crystal) $= 1.78\%$; R_I (magnetic) $= 1.90\%$						
$\mu_{Fe1} = 3.36(19)\,\mu_B$; $\mu_{Fe2} = 3.80(12)\,\mu_B$; $\mu_{Pr} = 0.83(20)\,\mu_B$						
Ba(1)	2*a*	1.0	0	0	0[a]	0.31 (8)
Ba(2)	6*c*	1.0	0.1738 (3)	0.8262	0.1600 (17)	0.31
Ba(3)	2*b*	1.0	1/3	2/3	0.4750 (18)	0.31
Ba(4)	6*c*	0.33333	0.4788 (3)	0.5212	0.8260 (16)	0.31
Pr	6*c*	0.66667	0.4788	0.5212	0.8260	0.31
Fe(1)	2*b*	1.0	1/3	2/3	0.0197 (17)	0.63 (7)
Fe(2)	6*c*	1.0	0.1772 (1)	0.8228	0.6597 (16)	0.63
O(1)	12*d*	1.0	0.6741 (5)	0.0656 (4)	0.0227 (15)	1.2 (1)
O(2)	6*c*	1.0	0.2501 (3)	0.7499	0.8383 (19)	1.2
O(3)	6*c*	1.0	0.4141 (3)	0.5859	0.1681 (18)	1.2
O(4)	6*c*	1.0	0.9024 (3)	0.0976	0.2711 (18)	1.2

[a] Fixed to zero.

Table 2
Structural parameters for $Ba_6Nd_2Fe_4O_{15}$ determined by the neutron diffraction measurements at 50 and 2.5 K.

Atom	Site	Occupancy	X	y	Z	B/Å^2
$T = 50$ K						
Space group $P6_3mc$; $a = 11.8176(10)$ Å, $c = 7.0184(5)$ Å						
$R_{wp} = 5.07\%$; $R_e = 3.30\%$; $R_I = 1.67\%$						
Ba(1)	2*a*	1.0	0	0	0[a]	0.34 (7)
Ba(2)	6*c*	1.0	0.1735 (2)	0.8265	0.1594 (15)	0.34
Ba(3)	2*b*	1.0	1/3	2/3	0.4726 (16)	0.34
Ba(4)	6*c*	0.33333	0.4787 (2)	0.5213	0.8265 (14)	0.34
Nd	6*c*	0.66667	0.4787	0.5213	0.8265	0.34
Fe(1)	2*b*	1.0	1/3	2/3	0.0164 (15)	0.77 (7)
Fe(2)	6*c*	1.0	0.1773 (1)	0.8227	0.6570 (15)	0.77
O(1)	12*d*	1.0	0.6729 (4)	0.0647 (3)	0.0208 (14)	1.2 (1)
O(2)	6*c*	1.0	0.2495 (3)	0.7505	0.8351 (17)	1.2
O(3)	6*c*	1.0	0.4149 (3)	0.5851	0.1638 (16)	1.2
O(4)	6*c*	1.0	0.9028 (3)	0.0972	0.2694 (16)	1.2
$T = 2.5$ K						
Space group $P6_3mc$; $a = 11.8065(9)$ Å; $c = 7.0114(4)$ Å						
$R_{wp} = 5.25\%$; $R_e = 2.89\%$; R_I (crystal) $= 1.38\%$; R_I (magnetic) $= 1.18\%$						
$\mu_{Fe1} = 3.19(17)\,\mu_B$; $\mu_{Fe2} = 3.95(10)\,\mu_B$; $\mu_{Nd} = 1.44(17)\,\mu_B$						
Ba(1)	2*a*	1.0	0	0	0[a]	0.44 (7)
Ba(2)	6*c*	1.0	0.1734 (3)	0.8266	0.1608 (16)	0.44
Ba(3)	2*b*	1.0	1/3	2/3	0.4751 (16)	0.44
Ba(4)	6*c*	0.33333	0.4788 (2)	0.5212	0.8260 (14)	0.44
Nd	6*c*	0.66667	0.4788	0.5212	0.8260	0.44
Fe(1)	2*b*	1.0	1/3	2/3	0.0176 (16)	0.73 (6)
Fe(2)	6*c*	1.0	0.1775 (1)	0.8225	0.6570 (15)	0.73
O(1)	12*d*	1.0	0.6731 (4)	0.0647 (4)	0.0210 (14)	1.3 (1)
O(2)	6*c*	1.0	0.2495 (3)	0.7505	0.8356 (18)	1.3
O(3)	6*c*	1.0	0.4149 (3)	0.5851	0.1645 (17)	1.3
O(4)	6*c*	1.0	0.9031 (3)	0.0969	0.2693 (17)	1.3

[a] Fixed to zero.

Curie term (χ_{Ln}):

$$\chi_M = \chi_{cluster} + 2\chi_{Ln} \quad (3)$$

In order to determine J_i, we tried to fit the experimental data ($T > 200$ K) using this equation with fixing the effective magnetic moment of the Ln^{3+} ion to the free-ion value because of a strong correlation between fitting parameters. The magnetic susceptibility calculated by this model is shown as a solid line in Fig. 4, and it is in good agreement with the experimental data. The J_1 and J_2 values are determined to be $-38.0(5)$ and $-3.4(1)$ K for Ln = Pr and $-38.9(6)$ and $-3.4(1)$ K for Nd, which are very close to those for the La compound ($-35.1(1)$ and $-3.41(2)$ K) [11]. Negative J values show that all the magnetic interactions between Fe^{3+} ions in the cluster are antiferromagnetic. From the determined J_1 and J_2 values, the magnetic ground state of the Fe_4O_{15} cluster becomes ferrimagnetic ($S_T = 5$ and $S' = 15/2$). The large J_1 value indicates that the magnetic interaction via the Fe(1)–O(2)–Fe(2) pathway is predominant in this temperature region ($T > 200$ K). The deviation between experimental and fitting curves observed at lower temperatures is attributed to the magnetic interaction between clusters via the longer pathway Fe–O–O–Fe.

3.3. Magnetic transition at low temperatures

Figs. 6 and 7 show the magnetic susceptibility and specific heat of $Ba_6Pr_2Fe_4O_{15}$ and $Ba_6Nd_2Fe_4O_{15}$ at low temperatures. Both compounds show an anomaly at 23.2 and 17.8 K, respectively. From the previous work [11], it was found that $Ba_6La_2Fe_4O_{15}$ shows an antiferromagnetic transition at 12.8 K, which is due to the long-range magnetic ordering of the cluster moments. The magnetic anomalies observed in the Pr and Nd compounds may also suggest the occurrence of the similar antiferromagnetic transition. In addition, the observed transition temperature is higher than that for the La compound, which indicates that the Ln^{3+} ions cooperate in this magnetic ordering.

The magnetic entropy change ΔS_{mag} associated with the magnetic transition was estimated from the specific heat data. The magnetic specific heat C_{mag} was calculated by subtracting the lattice specific heat from the experimental one. For the lattice contribution, the data of an isostructural and non-magnetic compound $Ba_6La_2Ga_4O_{15}$ [11] were used. The temperature dependence of the magnetic entropy calculated from $\int(C_{mag}/T)\,dT$ is plotted in Figs. 6(b) and 7(b). The magnetic entropy change at 40 K is 18.7 J mol^{-1} K^{-1} for $Ba_6Pr_2Fe_4O_{15}$ and 26.7 J mol^{-1} K^{-1} for $Ba_6Nd_2Fe_4O_{15}$.

At low temperatures, the ground state ($S_T = 5$, $S' = 15/2$) of the Fe_4O_{15} cluster is selectively populated (>95% at 40 K); in this case, the ΔS_{mag} for the magnetic ordering of the clusters is expected to be $R\ln(2S_T+1) = 19.9$ J K^{-1} mol^{-1}. This value is comparable with the experimental one for the $Ba_6La_2Fe_4O_{15}$ (18.2 J mol^{-1} K^{-1} at 40 K) [11]. The ΔS_{mag} for the Pr and Nd compounds are somewhat larger than that for the La compound; thus, the contribution from the Ln ions also exists. The increment in the Nd compound (~8.5 J mol^{-1} K^{-1}) is near to $2R\ln 2 = 11.5$ J K^{-1} mol^{-1} expected from the ground Kramers' doublet of the Nd^{3+} ion. On the other hand, the slight increment in the Pr compound (0.5 J mol^{-1} K^{-1}) may due to the fact that the Pr^{3+} is a non-Kramers ion and often have a singlet ground state.

Table 3
Some selected bond lengths and bond valence sums for $Ba_6Ln_2Fe_4O_{15}$ (Ln = Pr and Nd) determined by the neutron diffraction measurements at 50 K.

	$Ba_6Pr_2Fe_4O_{15}$ (50 K)		$Ba_6Nd_2Fe_4O_{15}$ (50 K)	
	Bond lengths (Å)	BVS	Bond lengths (Å)	BVS
Ba(1)–O(4) *x*3	2.565 (9)	2.25	2.565 (9)	2.27
Ba(1)–O(4) *x*3	2.755 (10)		2.745 (10)	
Ba(2)–O(2) *x*1	2.740 (10)	1.69	2.758 (10)	1.70
Ba(2)–O(3) *x*2	2.833 (5)		2.834 (5)	
Ba(2)–O(1) *x*2	2.869 (5)		2.874 (5)	
Ba(2)–O(1) *x*2	3.034 (8)		3.008 (8)	
Ba(2)–O(4) *x*1	3.153 (10)		3.151 (10)	
Ba(2)–O(4) *x*2	3.194 (6)		3.178 (5)	
Ba(3)–O(3) *x*3	2.724 (9)	1.73	2.736 (9)	1.71
Ba(3)–O(2) *x*3	3.072 (10)		3.069 (10)	
Ba(3)–O(1) *x*6	3.240 (4)		3.202 (4)	
Ba(4)/Ln –O(1) *x*2	2.448 (6)	3.67 (Ba)	2.414 (5)	3.86 (Ba)
Ba(4) –O(3) *x*1	2.477 (9)	2.47 (Pr)	2.459 (8)	2.37 (Nd)
Ba(4) –O(2) *x*2	2.587 (5)		2.588 (3)	
Ba(4)–O(3) *x*1	2.742 (9)		2.703 (8)	
Ba(4)–O(1) *x*2	2.723 (7)		2.722 (5)	
Fe(1) –O(3) *x*3	1.949 (7)	2.88	1.965 (7)	2.80
Fe(1)–O(2) *x*3	2.137 (8)		2.137 (8)	
Fe(2) –O(4) *x*1	1.819 (7)	3.01	1.819 (7)	2.99
Fe(2)–O(1) *x*2	1.851 (5)		1.861 (5)	
Fe(2)–O(2) *x*1	1.949 (8)		1.936 (8)	

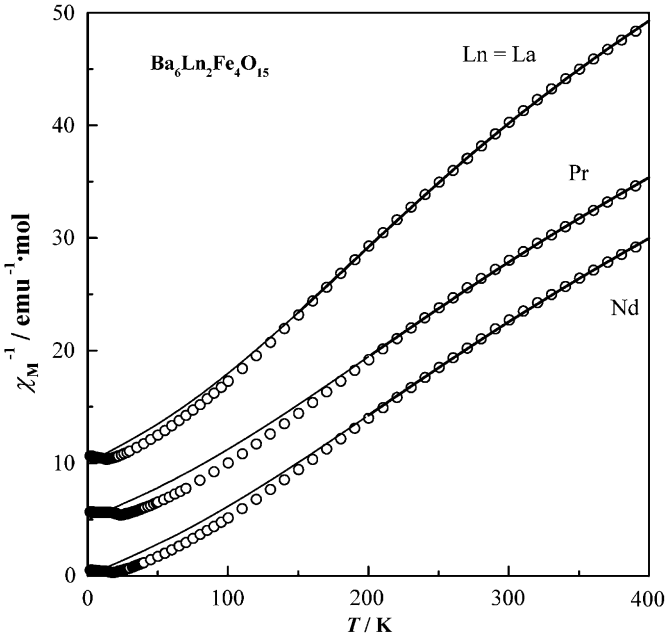

Fig. 4. Temperature dependence of the inverse magnetic susceptibility for $Ba_6Ln_2Fe_4O_{15}$. The solid lines represent the fitting curves using Eq. (3). Vertical offsets (10 emu^{-1} mol for Ln = La and 5 emu^{-1} mol for Pr) were added to avoid overlap.

3.4. Magnetization measurement

The magnetization vs. magnetic field curves for $Ba_6Ln_2Fe_4O_{15}$ at 1.8 K are plotted in Fig. 8. All the data show a saturation-like behavior above ~2 T. This result indicates that, by applying the magnetic field, the antiferromagnetic state by the Fe_4O_{15} clusters changes to the ferromagnetic one. In fact, the magnetization for $Ba_6La_2Fe_4O_{15}$ reaches 8.9 μ_B at 5 T [11], which is close to 10 μ_B expected from the ferromagnetic ordering of clusters with $S_T = 5$. The Pr and Nd compounds show larger values (10.7 and 11.7 μ_B, respectively) than that for the La compound. This increase is attributed to the contribution from the magnetic moments of Ln^{3+} ions.

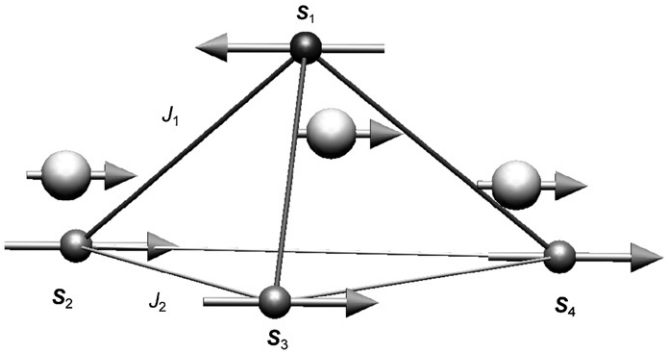

Fig. 5. The spin arrangement of the magnetic Fe_4O_{15} cluster and Ln ions. The larger white circles represent the *Ln* ions in the Ba(4)/*Ln* site and smaller circles represent the Fe(1) (black) and Fe(2) (gray) ions.

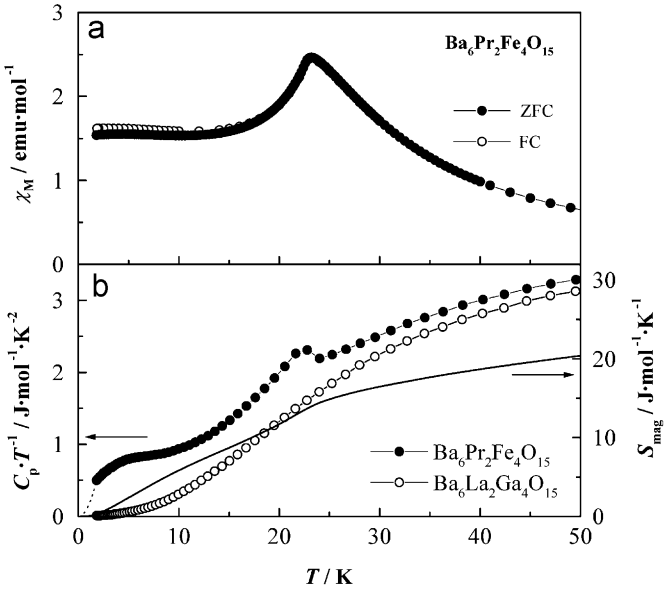

Fig. 6. Temperature dependence of (a) magnetic susceptibility (χ_M) and (b) specific heat divided by temperature (C_p/T) and magnetic entropy (S_{mag}) for $Ba_6Pr_2Fe_4O_{15}$.

3.5. Magnetic structure

The powder neutron diffraction profiles for $Ba_6Pr_2Fe_4O_{15}$ and $Ba_6Nd_2Fe_4O_{15}$ at 2.5 K are shown in Figs. 2(b) and 3(b), respectively. In both data, magnetic reflections were observed at lower angles, which were not observed at 50 K. They were all indexed by using a propagation vector $\boldsymbol{k} = (1/2, 0, 0)$ indicating the magnetic unit cell with $a_{mag} = 2a$, $b_{mag} = b$, and $c_{mag} = c$. In order to determine the magnetic structure, we assumed that each Fe_4O_{15} cluster is in a ground state, i.e., the magnetic moment of the Fe(1) ion is antiparallel to three Fe(2) magnetic moments in a cluster. The best fit was obtained when (i) two cluster moments in a crystal unit cell are parallel with each other and they

order antiferromagnetically according to the ***k*** vector, (ii) the magnetic moments of *Ln* ions are parallel to that of the nearest cluster (see Fig. 5), and (iii) all the magnetic moments are collinear along the *b*-axis. The determined magnetic structure is illustrated in Fig. 9, and the refined structural parameters are listed in Tables 1 and 2.

The magnetic structures determined for $Ba_6Pr_2Fe_4O_{15}$ and $Ba_6Nd_2Fe_4O_{15}$ can be regarded as an antiferromagnetic ordering of the cluster moments, which is the same with the case of $Ba_6La_2Fe_4O_{15}$ [11]. Fig. 10 illustrates this magnetic structure by using the cluster moments. The cluster moments order ferromagnetically along the *c*-axis, i.e., ferromagnetic cluster chains are formed. These chains make a honeycomb-like array on the *c*-plane, and the magnetic moments of the chains order antiferromagnetically. The deviation between the observed and calculated magnetic suscept-

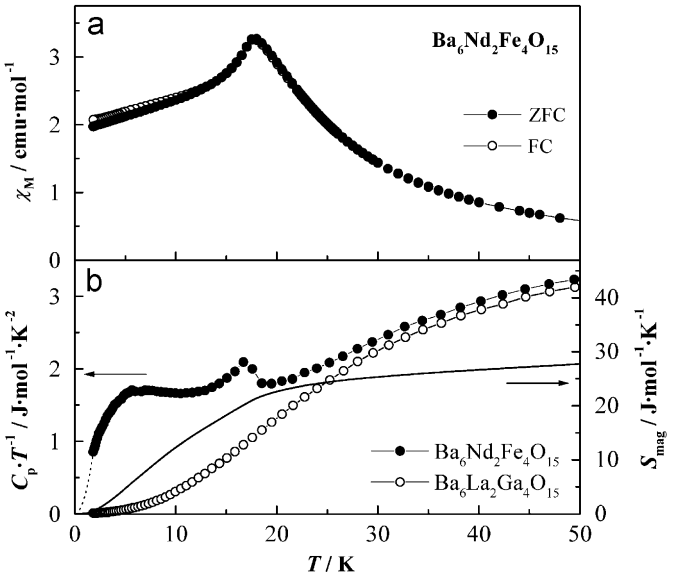

Fig. 7. Temperature dependence of (a) magnetic susceptibility (χ_M) and (b) specific heat divided by temperature (C_p/T) and magnetic entropy (S_{mag}) for $Ba_6Nd_2Fe_4O_{15}$.

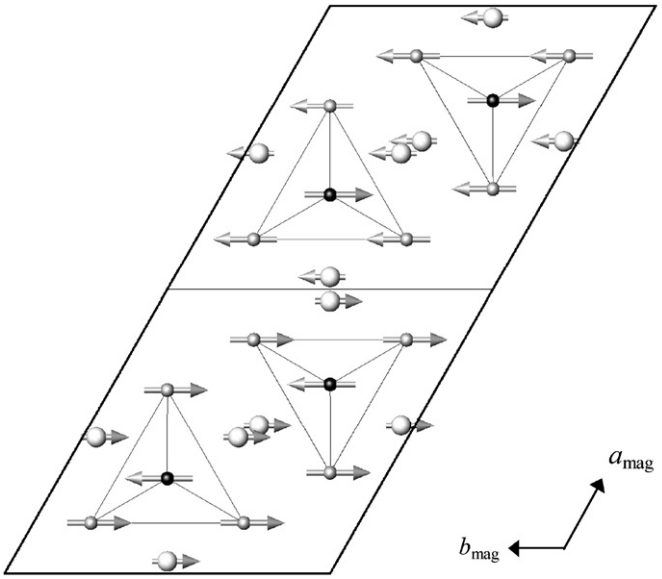

Fig. 9. Magnetic structure of $Ba_6Ln_2Fe_4O_{15}$ (*Ln* = Pr and Nd). Larger white circles: *Ln*; smaller black and gray circles: Fe(1) and Fe(2), respectively. Note that the site occupation of *Ln* ions is 2/3.

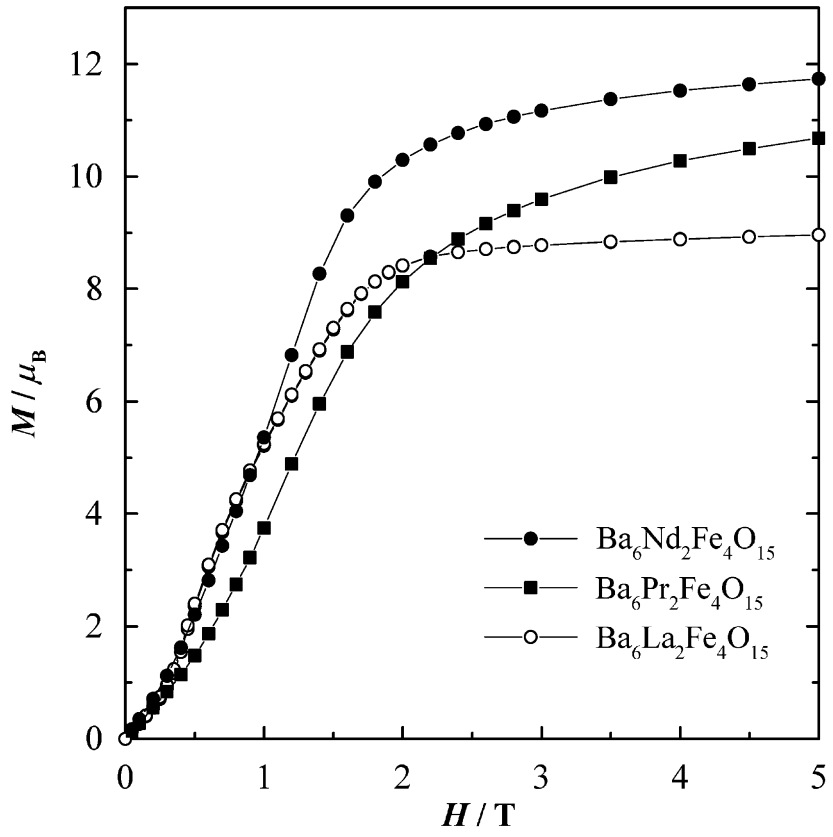

Fig. 8. Field dependence of the magnetization for $Ba_6Ln_2Fe_4O_{15}$ (*Ln* = Pr and Nd) at 1.8 K.

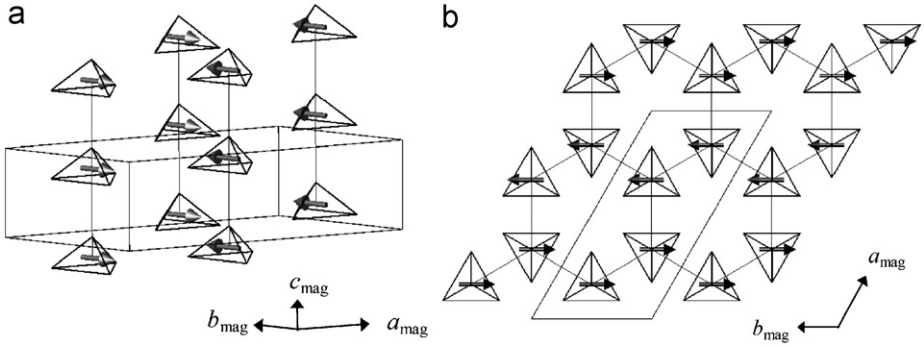

Fig. 10. Magnetic structure of $Ba_6Ln_2Fe_4O_{15}$ (Ln = Pr and Nd) represented by using the cluster moments: (a) the cluster chain along the c-axis and (b) the honeycomb array of the chains on the c-plane.

ibilities (Fig. 4) may indicate that the onset of the ferromagnetic ordering in the cluster chain occurs above the Néel temperature (T_N).

In the temperature region below T_N, the nearest chains adopt both antiferromagnetic and ferromagnetic arrangements in the ratio 1:2 (see Fig. 10). The honeycomb lattice itself is geometrically unfrustrated [16], and all of the nearest pairs can adopt an antiferromagnetic (ferromagnetic) arrangement when an antiferromagnetic (ferromagnetic) interaction between the nearest chains is predominant. Therefore, the observed magnetic structure indicates that there is a competition in the magnetic interaction, conceivably, between the nearest (ferromagnetic) and next-nearest (antiferromagnetic) chains. In fact, by applying a relatively small magnetic field (~2 T), the antiferromagnetic ordering of the chains changes to the ferromagnetic one, which means that the nearest interaction gets an advantage. The ordered magnetic moments for each Fe^{3+} ion are 3.2–4.0 μ_B; these values are smaller than the 5 μ_B expected from the high spin state ($S = 5/2$). This result may arise from this competition.

The magnetic structures for $Ba_6Pr_2Fe_4O_{15}$ and $Ba_6Nd_2Fe_4O_{15}$ show that the magnetic moments of the Ln^{3+} ions are also ordered. The ordered moment is parallel to the ferrimagnetic moment of the nearest Fe_4O_{15} cluster, and acts in concert with the cluster moment when the magnetic field is applied. The ordered moments are determined to be 0.83(20) μ_B for Ln = Pr and 1.44(17) μ_B for Nd. Both are much smaller than $g_J J$(3.20 and 3.27 μ_B, respectively), which is mainly due to the crystal field effect. The small magnetic entropy change for the Pr^{3+} ion (~0.25 J mol^{-1} K^{-1} per Pr^{3+}) in the $Ba_6Pr_2Fe_4O_{15}$ indicates the singlet ground state. The non-zero ordered moment may be induced by the internal magnetic field which is produced by the cluster moment.

Acknowledgments

This research was partially supported by the Ministry of Education, Culture, Sports, Science and Technology, Japan, the Scientific Research Priority Areas "Panoscopic Assembling and High Ordered Functions for Rare Earth Materials" (19018003).

References

[1] T. Lis, Acta. Crystallogr. B 36 (1980) 2042–2046.
[2] A. Caneschi, D. Gatteschi, R. Sessoli, A.L. Barra, L.C. Brunel, M. Guillot, J. Am. Chem. Soc. 113 (1991) 5873–5874.
[3] J. Darriet, M. Drillon, G. Villeneuve, P. Hagenmuller, J. Solid State Chem. 19 (1976) 213–220.
[4] J. Darriet, J.L. Soubeyroux, A.P. Murani, J. Phys. Chem. Solids 44 (1983) 269–272.
[5] D.A. Vander Griend, S. Boudin, V. Caignaert, K.R. Poppelmeier, Y. Wang, V.P. Dravid, M. Azuma, M. Takano, Z. Hu, J.D. Jorgensen, J. Am. Chem. Soc. 121 (1999) 4787–4792.
[6] M. Azuma, T. Okada, M. Takano, D.A. Vander Griend, K.R. Poppelmeier, Y. Narumi, K. Kindo, Y. Mizuno, S. Maekawa, Phys. Rev. B 62 (2000) R3588.
[7] H. Mevs, H.k. Müller-Buschbaum, J. Less-common Met. 157 (1990) 173–178.
[8] H. Mevs, H.k. Müller-Buschbaum, J. Less-common Met. 158 (1990) 147–152.
[9] D.A. Kudryavtsev, B.V. Mill', N.F. Vedernikov, I.S. Shaplygin, Inorg. Mater. 28 (1992) 943–946.
[10] H.k. Müller-Buschbaum, S. Meyer, Z. Anorg. Allg. Chem. 623 (1997) 200–204.
[11] K. Abe, Y. Doi, Y. Hinatsu, K. Ohoyama, Chem. Mater. 18 (2005) 785–789.
[12] I. Rüter, H.k. Müller-Buschbaum, Monatsh. Chem. 120 (1989) 1069–1074.
[13] K. Ohoyama, T. Kanouchi, K. Nemoto, M. Ohashi, T. Kajitani, Y. Yamaguchi, Jpn. J. Appl. Phys. 37 (1998) 3319–3326.
[14] F. Izumi, T. Ikeda, Mater. Sci. Forum 321-324 (2000) 198–203.
[15] I.D. Brown, A. Altermatt, Acta Crystallogr. B 41 (1985) 244–247.
[16] A. Harrison, J. Phys. Condens. Matter 16 (2004) S553–S572.